Air cushioning in droplet impacts with liquid layers and other droplets

Peter D. Hicks and Richard Purvis

Citation: Physics of Fluids **23**, 062104 (2011); doi: 10.1063/1.3602505
View online: http://dx.doi.org/10.1063/1.3602505
View Table of Contents: http://scitation.aip.org/content/aip/journal/pof2/23/6?ver=pdfcov
Published by the AIP Publishing

Air cushioning in droplet impacts with liquid layers and other droplets

Peter D. Hicks[a] and Richard Purvis[b]
School of Mathematics, University of East Anglia, Norwich NR4 7TJ, United Kingdom

(Received 20 May 2010; accepted 18 May 2011; published online 28 June 2011)

Air cushioning of a high-speed liquid droplet impact with a finite-depth liquid layer sitting upon a rigid impermeable base is investigated. The evolution of the droplet and liquid-layer free-surfaces is studied alongside the pressure in the gas film dividing the two. The model predicts gas bubbles are trapped between the liquid free-surfaces as the droplet approaches impact. The key balance in the model occurs when the depth of the liquid layer equals the horizontal extent of interactions between the droplet and the gas film. For liquid layer depths significantly less than this a shallow liquid limit is investigated, which ultimately tends towards the air-cushioning behavior seen in droplet impact with a solid surface. Conversely, for liquid layer depths much deeper than this, the rigid base does not affect the air-cushioning of the droplet. The influence of compressibility is discussed and the relevant parameter regime for an incompressible model is identified. The size of the trapped gas bubble as a function of the liquid layer depth is investigated. The deep water model is extended to consider binary droplet collisions. Again, the model predicts gas bubbles will be trapped as the result of air cushioning in high-speed binary droplet impacts. © *2011 American Institute of Physics*. [doi:10.1063/1.3602505]

I. INTRODUCTION

In many physical situations droplets impinge on a layer of liquid covering a rigid surface. Practical examples include raindrops landing in puddles or during industrial coating processes. As touchdown is approached during a violent, high-speed droplet impact, air-cushioning slows the droplet descent and deforms both the droplet and liquid layer free-surfaces. This allows a pocket of gas to become trapped at the site of the droplet impact. Experiments have shown that this pocket of gas can subsequently evolve into a bubble,[1] entraining gas within the liquid phase. In spray coating these bubbles may be detrimental to the quality of finish of the final surface, while air bubbles trapped by raindrops landing on water provide a mechanism through which gases (including airborne contaminants and pollutants) can be transferred to the water.[2]

In addition to bubbles trapped by air cushioning between a droplet and a liquid layer, experimental studies have also shown that gas bubbles can be created as the result of air cushioning during droplet impact with a rigid surface.[3,4] In air-cushioned droplet impact experiments, in addition to the large central bubble, much smaller bubbles have also been seen at a greater radius from the center of the impact in a phenomena called Mesler entrainment.[5,6] This is inferred to be the result of capillary interactions between the droplet and liquid layer free-surfaces. In addition to air cushioning, a gas bubble may become entrained during a droplet impact due to the collapse of an impact crater.[7]

The result of a droplet impact depends on many physical parameters including the properties of the fluid forming the droplet, the speed of approach to impact, and the droplet radius. When a droplet impacts a liquid layer, the depth of liquid has a significant effect on the resulting air cushioning and the splash dynamics. We seek to investigate how the depth of the receptor fluid affects the evolution of the free-surfaces and the resulting volume of the trapped bubble, when both the droplet and the liquid layer consist of the same fluid. For a sufficiently deep liquid layer the air cushioning of the droplet is not affected by the bottom of the liquid layer. However, for a shallower liquid layer the presence of the impermeable base has an increasing effect on the free-surface evolution. A limiting case is reached in which the liquid layer thickness tends to zero and the droplet impacts a solid surface. The evolution of the droplet and layer free-surfaces, and the resulting bubble volume as the depth of the receptor fluid varies, forms the focus of the present study.

The evolution of the gas pressure in the region separating a liquid and a solid body approaching impact was first described by Verhagen,[8] who considered the evolution of a slowly varying one-dimensional gas channel between a liquid and a solid body, in the context of ship slamming and wave impacts. In this parameter regime Wilson[9] formally derived a model in which both the liquid and gas phases are inviscid. This model was later shown to be unstable to small perturbations in the initial conditions.[10,11] However, interest remains into traveling wave solutions in this system.[12,13]

The length scales associated with droplet impacts are much smaller than those associated with ship slamming, although the liquid velocities may be equally large. For high momentum droplets with Reynolds numbers greater than $O(10^7)$, Smith *et al.*[14] showed that the inviscid model of Wilson[9] is appropriate for describing air cushioning. However, for lower Reynolds numbers a viscous description of the gas was shown to be appropriate, giving a model for the gas based upon lubrication theory. This was coupled to an inviscid description of the droplet and used to study air cushioning phenomena. In normal impacts, the narrowing of the gas film as the droplet approaches impact is a canonical

[a]Electronic mail: p.hicks@uea.ac.uk.
[b]Electronic mail: r.purvis@uea.ac.uk.

squeeze film problem in which the evolution of free surface and pressure are determined through coupling with the inviscid droplet behavior. As one would expect, high pressures in the gas film are initially generated where the separation distance between the droplet and the solid is least. Subsequently these high pressures act to decelerate the droplet and locally deflect the free-surface away from the point of impact. Air cushioning, therefore, acts to slow the droplet immediately prior to impact, while the deformed free-surface touches down at some horizontal distance away from the bottom of the droplet, thus trapping a gas bubble. Similar behavior is to be expected in the case of a liquid layer, when an equivalent lubrication equation governs the gas pressure in a film trapped between the two free-surfaces.

The model of Smith *et al.*[14] was initially proposed to describe the idealized two-dimensional normal impact problem with incompressible liquid and gas phases, in the absence of surface tension effects. Subsequent extensions to the basic model have incorporated surface tension,[11,15] oblique impacts,[16–18] compressibility,[15] and three-dimensional effects,[18] extending the range of validity.

If the air phase is neglected completely, then two-dimensional impact problems typically lead to co-dimension two free-boundary problems. Asymptotic analyses for solid-deep water impacts,[10,19,20] solid-shallow water impact,[21] and droplet-liquid layer impact[22,23] show liquid jet initiation close to the point of impact which has the potential to evolve into the characteristic splash seen in many impacts. However, in models which neglect the air phase, the liquid remains completely stationary or in uniform motion, right until the point of initial touchdown, in contradiction to the air-cushioning experiments and analysis. Therefore, a greater understanding of air-cushioning pre-impact phenomena is a key to generating more realistic initial conditions for studying post impact behavior.

At lower approach speeds, viscous and surface tension effects become significant, leading to many other styles of impact behavior including more gradual coalescence and droplet spreading rather than splashing. This regime has been considered for droplet impact with a solid[24] and for droplet impact with a liquid layer.[25] With even stronger surface tension effects the entire droplets can bounce off the liquid body they come into contact, with no mass transfer between the two.[26]

In addition to droplet impact with a liquid layer, the current study extends the model to consider high-speed impact between a pair of droplets. At slower approach speeds, droplet coalescence is a widely studied problem.[27] In this slower regime the draining of the film separating the droplets is a direct analogue of the air cushioning we see in higher speed impacts. The film draining behavior can be modeled by a viscous lubrication approximation, albeit this time coupled to viscous (rather than inviscid) liquid droplet behavior. The free-surface profiles generated by these models are markedly similar to those seen in air cushioning, with the minimum separation distance again occurring some horizontal distance away from the centerline of the two droplets.[28,29]

In Sec. II, a model is derived governing the behavior of a two-dimensional liquid droplet approaching a finite depth layer of the same liquid, which itself is resting upon a rigid surface. The role gas plays in the narrowing gap that results as the droplet approaches impact is investigated. Section III includes profiles for a range of liquid layer depths, along two distinguished limits corresponding to the cases in which the depth of the receptor liquid is much greater and much smaller than the horizontal extent of the interactions between gas film and the free surfaces. The effect of the liquid layer depth on the volume of the trapped air pocket is considered in Sec. IV, while Sec. V extends the model to look at air cushioning in binary droplet collisions. Conclusions and further discussions are given in Sec. VI.

II. MODEL FORMULATION

The role gas cushioning plays as a liquid droplet approaches impact with a thin layer of the same liquid is investigated by considering an initially undisturbed droplet with radius R and approaching impact with a liquid layer of depth H, from a direction perpendicular to the layer with an approach speed U_0. The liquid layer rests upon a rigid impermeable base. Our primary interest is in the period immediately prior to impact when the two liquid bodies are separated by a narrow gas film.

In the experiments of Thoroddsen *et al.*,[1] droplets of radius 2 mm impact into a liquid layer at speeds between 0.49 and 3.84 m s^{-1}. This gives a Reynolds number, $Re = \rho_l R U_0/\mu_l$, of between 1000 and 8000, a range significantly below the inviscid-inviscid regime described by Smith *et al.*[14] Here the fluid density is denoted by ρ and viscosity by μ, while the subscript l denotes a property of the liquid phase. These experiments are conducted with a water layer whose depth is much greater than the horizontal extent of the pre-impact interactions between the droplet and the water. A second set of experiments by Thoroddsen *et al.*[3] also shows bubble capturing droplet impacts, albeit this time during impact with a solid surface. These experiments were also conducted within a similar range of Reynolds numbers. The impact experiments for droplet impact with deep water and for droplet impact with a solid provide two limiting cases in which the typical size of a trapped bubble can be measured. We wish to investigate air cushioning as the layer depth varies between these two limiting cases.

The idealized problem of a two-dimensional normal impact in which a circular droplet approaches an initially stationary liquid layer is investigated. A coordinate system with its origin located on the undisturbed layer free-surface directly below the center of the droplet is used. The $\hat{x}$ coordinate lies parallel to the layer, and the $\hat{y}$-coordinate is positive in the direction of the droplet (see Figure 1). The upper boundary between the droplet and the gas filled gap is denoted $\hat{y} = \hat{f}^+(\hat{x}, \hat{t})$, and the lower boundary between the gap and the liquid layer is denoted $\hat{y} = \hat{f}^-(\hat{x}, \hat{t})$.

It is assumed that both fluid flows are governed by the Navier-Stokes equations. Additionally, the liquid phase is assumed to be incompressible. The model equations are non-dimensionalized using R and R/U_0 as the length and time scales, respectively. The dimensionless liquid pressure $\hat{p}_l$ is assumed to be related to the dimensional liquid pressure $\bar{p}_l$ through $\bar{p}_l = p_0 + \rho_l U_0^2 \hat{p}_l$, where p_0 is the surrounding ambient pressure. These scalings result in non-dimensional Navier-Stokes equations for the liquid phase with the form

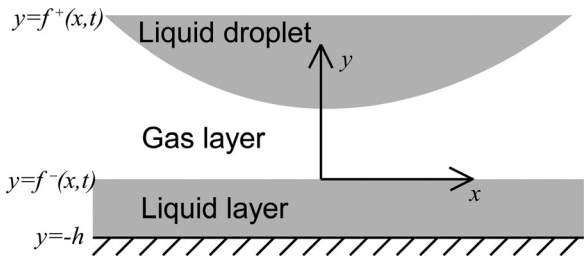

FIG. 1. Schematic of a liquid droplet with free surface $y=f^{+}(x,t)$, approaching impact with a shallow liquid layer whose free surface is given by $y=f^{-}(x,t)$.

$$\hat{\nabla}\cdot\hat{u}_l = 0, \tag{1a}$$

$$\frac{\partial \hat{u}_l}{\partial \hat{t}} + \hat{u}_l\cdot\hat{\nabla}\hat{u}_l = -\hat{\nabla}\hat{p}_l + \frac{1}{Re}\hat{\nabla}^2\hat{u}_l. \tag{1b}$$

In the gas, compressibility effects are initially retained, and their importance investigated. In addition to the scales in the liquid, the dimensional gas density $\bar{\rho}_g$ and pressure $\bar{p}_g$ are related to their dimensionless counterparts $\hat{\rho}_g$ and $\hat{p}_g$ through $\bar{\rho}_g = [\rho_g]\hat{\rho}_g$ and $\bar{p}_g = p_0 + \rho_l U_0^2 \hat{p}_g$, respectively. Here the subscript g denotes a property of the gas phase, and the scaling for the gas pressure is chosen to match with the liquid phase. Together with the scalings for the liquid phase this implies

$$\frac{\partial \hat{\rho}_g}{\partial t} + \hat{\nabla}\cdot\left(\hat{\rho}_g\hat{u}_g\right) = 0, \tag{2a}$$

$$\frac{[\rho_g]\hat{\rho}_g}{\rho_l}\left(\frac{\partial \hat{u}_g}{\partial \hat{t}} + \hat{u}_g\cdot\hat{\nabla}\hat{u}_g\right) = -\hat{\nabla}\hat{p}_g + \frac{\mu_g}{\mu_l}\frac{1}{Re}\hat{\nabla}^2\hat{u}_g + \frac{\mu_g}{\mu_l}\frac{\Gamma}{Re}\hat{\nabla}\left(\hat{\nabla}\cdot\hat{u}_g\right), \tag{2b}$$

where the viscosity ratio $\Gamma = (\lambda_g + \mu_g)/\mu_g$, and λ_g is the dilatational viscosity in the gas. Here it is assumed that the viscosity of the gas is constant.

To complete this system an equation of state and an energy conservation equation are required to determine the gas temperature. In dimensional variables, if the gas is governed by the ideal gas law, the equation of state is given by

$$\bar{p}_g = \bar{\rho}_g R_g \bar{T}_g, \tag{3}$$

where the absolute dimensional gas temperature and the specific gas constant of the gas film are denoted $\bar{T}_g$ and R_g, respectively. The dimensional energy conservation equation may be written as

$$\bar{\rho}_g c_{v,g}\frac{D\bar{T}_g}{D\bar{t}} + \bar{p}_g\overline{\nabla}\cdot\mathrm{u}_g = k_g\overline{\nabla}^2\bar{T}_g + \bar{\Phi}, \tag{4}$$

where $c_{v,g}$ is the specific heat of the gas at constant volume, k_g is the thermal diffusivity of the gas, and $\bar{\Phi}$ is the dissipation.[30] The terms in this equation correspond to the rate of change of thermal energy, the work done by pressure, the diffusion of heat, and the heat generated by viscous effects. The dissipation is given by

$$\bar{\Phi} = \lambda_g\left(\overline{\nabla}\cdot\bar{\mathbf{u}}_g\right)^2 + \frac{\mu_g}{2}\left(\frac{\partial \bar{u}_i}{\partial \bar{x}_j} + \frac{\partial \bar{u}_j}{\partial \bar{x}_i}\right)^2, \tag{5}$$

with the usual summation convention. In a viscous gas flow, the dissipation and the thermal diffusion terms on the right-hand side of Eq. (4) may be comparable in size to the terms on the left-hand side of that equation and cannot be immediately neglected.

Following the approach of Howell,[31] further details of how thermal diffusion and viscous dissipation affect the model presented here are discussed in Sec. II D and the scaled, non-dimensional version of Eq. (4) is given in Appendix. The main implication of these terms for the incompressible model studied here is an additional restriction on the parameter values for which effects due to compressibility can be neglected. However, at this stage, for simplicity and to allow comparison with recent literature[15,32] we assume the effects of thermal diffusion and dissipation in Eq. (4) are small and can be neglected. In this case the equation of state simplifies to

$$\frac{\bar{p}_g}{p_0} = \left(\frac{\bar{\rho}_g}{\rho_0}\right)^{\gamma}, \tag{6}$$

where γ is the ratio of specific heats. Here ρ_0 is a reference gas density based on the ambient gas pressure. Therefore, in this case the equation of state is given by Eq. (6), and an explicit equation governing the temperature evolution is no longer required to close the model.

If the gas density scale $[\rho_g] = \rho_0$, then the equivalent dimensionless relationship to Eq. (6) is given by

$$\hat{\rho}_g = \left(1 + K\hat{p}_g\right)^{1/\gamma}, \tag{7}$$

where

$$K = \frac{\rho_l U_0^2}{p_0} \tag{8}$$

measures the importance of gas compressibility in the model. For large K, the variations in the gas film pressure are large compared to the ambient gas pressure, and therefore gas compressibility is significant.

On the interfaces between the liquid and gas, kinematic boundary conditions imply

$$\hat{v}_\alpha = \frac{\partial \hat{f}^{\pm}}{\partial \hat{t}} + \hat{u}_\alpha\frac{\partial \hat{f}}{\partial \hat{x}}, \quad \text{on } \hat{y} = \hat{f}^{\pm}(\hat{x},\hat{t}), \tag{9}$$

where $\alpha = l$ in the liquid or g in the gas, while the normal stress balance across the interface implies that the difference in the normal stresses between the liquid and the gas equals the curvature of the interface multiplied by the coefficient of surface tension σ. On the solid boundary $\hat{y} = -H$, the no-slip and no-penetration boundary conditions imply $\hat{u}_l|_{\hat{y}=-H} = \hat{v}_l|_{\hat{y}=-H} = 0$.

A time origin is chosen so that touchdown of the droplet onto the liquid layer would occur at $\hat{t} = 0$ in the absence of gas cushioning. For large negative time, the non-dimensional undeformed droplet and liquid layer are assumed to satisfy

$$\hat{f}^{+} = -\sqrt{1-\hat{x}^2} - \hat{t} + 1, \tag{10a}$$

$$\hat{f}^{-} = 0, \tag{10b}$$

while the non-dimensional pressure in the gap is initially taken to be zero. Throughout the evolution, the droplet and

liquid layer free-surfaces are assumed to approach their undeformed profiles, a long way from the region of interaction. Also, in the far field the pressure disturbance decays to zero. For the following analysis it is expedient to define the difference and sum of a property θ on the droplet and layer free-surfaces to be

$$[\theta] = \theta^+ - \theta^-, \quad \text{and} \quad \langle\theta\rangle = \theta^+ + \theta^-, \tag{11}$$

respectively.

A. Gas film

The gas occupying the narrow gap between the droplet and the liquid layer can be considered to be the fluid in a canonical squeeze film problem, albeit one in which both upper and lower boundaries are allowed to deform in response to the gas pressure in the gap. These boundaries form interfaces within the flow whose position is to be determined.

In addition to the droplet radius R, there exists a length scale L in the problem, corresponding to the horizontal extent of the interactions between the droplet and the liquid layer free-surfaces. The size of L is yet to be determined. However, we assume the aspect ratio

$$\varepsilon = \frac{L}{R} \tag{12}$$

is small, and like L the value of ε is to be determined. We are interested in the very short time behavior just prior to impact, which motivates a rescaling of time with $\hat{t} = \varepsilon^2 t$. At this stage the typical vertical separation between the free-surfaces is a factor ε smaller than the horizontal extent of the interactions. Therefore, in order to focus on the region close to the point of impact we take,

$$(\hat{x},\, \hat{y}) = \varepsilon(x,\, \varepsilon y). \tag{13a}$$

The difference in scaling the vertical height of the gas filled gap relative to its horizontal extent immediately forces the usual scaling on the velocity components in order to conserve mass. Therefore,

$$(\hat{u}_g,\, \hat{v}_g, \hat{f}^{\pm}, \hat{p}_g,\, \hat{\rho}_g) = \left(\varepsilon^{-1}U,\, V,\, \varepsilon^2 f^{\pm},\, \varepsilon^{-1}P,\, \rho\right) + \cdots, \tag{13b}$$

where variations in the free-surface heights are of the same size as the gap thickness, while the pressure and density are scaled to maintain their presence in the problem at leading order.

Following the earlier study by Hicks and Purvis,[18] we shall investigate the case in which there is a balance in the leading-order horizontal momentum conservation equation between the pressure gradient and the viscous terms, leading to the definition

$$\varepsilon = \left(\frac{\mu_g}{\mu_l Re}\right)^{1/3} \tag{14}$$

for the ratio of L to R. Further details of the choice of ε are given below, including the key assumptions on the sizes of the terms neglected. If substituted into the Navier-Stokes equations for the gas (Eq. (2)), then

$$\rho_t + (\rho U)_x + (\rho V)_y = 0, \tag{15a}$$

$$0 = -P_x + U_{yy}, \tag{15b}$$

$$0 = -P_y. \tag{15c}$$

Here the acceleration and inertia terms (of size $\rho_g U_0^2 \big/ \rho_l \varepsilon^3 R$) are assumed to be small compared to the terms involving the pressure gradient (of size $U_0^2/\varepsilon^2 R$). This scaling also removes all the terms involving the dilatational viscosity providing, $\varepsilon \ll \Gamma^{-1/2}$. Further restrictions on ε are given in the next section.

In the scaled coordinate system

$$f^+ = \frac{x^2}{2} - t, \quad f^- = 0, \quad \text{and} \quad P = 0, \tag{16}$$

for large negative t. Far-field conditions on the free-surfaces and pressure throughout the droplet approach are given by

$$f^+ \sim \frac{x^2}{2} - t,\ f^- \to 0,\ \text{and}\ P \to 0,\ \text{as}\ |x| \to \infty. \tag{17}$$

To leading order, the kinematic boundary conditions (9) imply

$$U = 0, \quad V = f_t^{\pm}, \quad \text{on } y = f^{\pm}(x,\, t). \tag{18}$$

Momentum conservation in the vertical direction (Eq. (15c)) immediately implies $P = P^{\pm} = P(x,t)$, with the consequence that

$$[P] = P^+ - P^- = 0. \tag{19}$$

Upon integrating between the two interfaces f^- and f^+, a lubrication equation is recovered, relating the pressure in the gap to the free-surface positions. This has the form

$$12(\rho[f])_t = (\rho[f]^3 P_x)_x, \tag{20}$$

where $[f] = f^+ - f^-$ is the difference in height between the two fluid surfaces.

B. Droplet and layer deformation

In the liquid phase, we again wish to focus on the region close to impact and accordingly scale time with $\hat{t} = \varepsilon^2 t$, and the spatial coordinates with $(\hat{x},\, \hat{y}) = \varepsilon(x,\, y)$. Notice, in the droplet and the layer the typical vertical length scale is assumed to be comparable to the horizontal length scale. Liquid mass conservation now dictates the velocity components are scaled with $(\hat{u}_l,\, \hat{v}_l) = (u,\, v)$, while $\hat{p}_l = \varepsilon^{-1} p$ to match the pressure in the gas and $\hat{f}^{\pm} = \varepsilon^2 f^{\pm}$ on the free-surfaces. If the non-dimensional Navier-Stokes equations for the liquid (Eq. (1)) are scaled in this way, then the leading order behavior in the droplet and the layer is governed by

$$u_x + v_y = 0, \tag{21a}$$

$$u_t = -p_x, \tag{21b}$$

$$v_t = -p_y, \tag{21c}$$

where the inertial and viscous terms (of size U_0/ε^2 and U_0, respectively) are assumed to be much smaller than the pressure gradient and acceleration terms (of size $\mu_l U_0/\rho_l \varepsilon^2 R^2$). With ε defined by Eq. (14), together with the assumptions inherent in Eq. (15), this means

$$\frac{\rho_g}{\rho_l} \ll \varepsilon \ll \left(\frac{\mu_g}{\mu_l}\right)^{1/3}, \tag{22}$$

providing an applicable range for ε. In the case of droplets impacting a water layer separated by air, the ratios of gas to liquid viscosity and density are approximately $1/100$ and $1/772$, respectively. If we differentiate Eq. (21) we find

$$v_{tx}(x, y, t) = -p_{xy}(x, y, t), \quad \text{and} \quad v_{ty}(x, y, t) = p_{xx}(x, y, t), \tag{23}$$

the Cauchy-Riemann equations for the functions $v_t(x,y,t)$ and $-p_x(x,y,t)$.

The kinematic boundary conditions on the free surfaces reduce to

$$v(x, y, t) \sim f_t^{\pm}(x, t), \quad \text{as} \quad y \to 0\pm, \tag{24a}$$

while

$$p(x, y, t) \sim p^{\pm}(x, t), \quad \text{as} \quad y \to 0\pm. \tag{24b}$$

Here, the plus (minus) on the free-surface position and the pressure refers to a property evaluated on the upper droplet (lower layer) free-surface. The presence of the rigid body at the base of the liquid layer results in a scaled no-penetration boundary condition of the form

$$v(x, y, t) = 0, \quad \text{on} \quad y = -h. \tag{25}$$

Here the scaled layer depth is related to the original dimensional layer depth through $h = H/\varepsilon R$. For a droplet with radius $R = 2$ mm and approach speed $U_0 = 1$ m s^{-1}, we find $\varepsilon = 0.0207$; so, a layer with non-dimensional depth $h = 1$ corresponds to a dimensional layer depth $H = 41.5$ μm. In comparison to this, the experiments of Thoroddsen *et al.*[1] are conducted with much deeper liquid layers.

To satisfy Eq. (25) directly, an image system in which there is an identical second free-surface whose undisturbed position is $y = -2h$ is introduced. The analytic complex function

$$w(x + iy, t) = p_x(x, y, t) + iv_t(x, y, t), \tag{26}$$

is constructed, which is bounded in the far field and has the properties

$$w(x \pm 0i, t) = p_x^{\pm}(x, t) + if_{tt}^{\pm}(x, t), \tag{27a}$$

$$w(x - 2hi \mp 0i, t) = p_x^{\pm}(x, t) - if_{tt}^{\pm}(x, t), \tag{27b}$$

when the boundary conditions (24) are applied. We next integrate around the contour shown in Figure 2 using Cauchy's integral formula evaluated at $x \pm 0i$. If the radius of the semi-circles in the contours is large, then,[22,33]

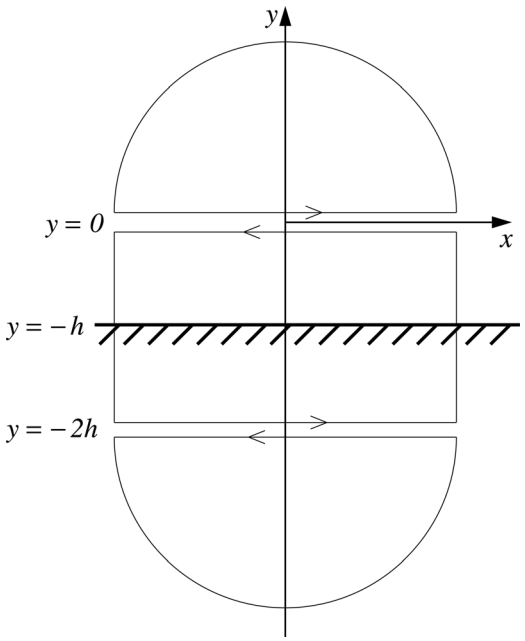

FIG. 2. Contour and image system used to solve the potential flow resulting from a droplet impact with a shallow liquid layer.

$$\langle p_x \rangle(x, t) = \frac{1}{\pi} \int_{-\infty}^{\infty} \frac{[f_{tt}](\xi, t)d\xi}{\xi - x} + \frac{1}{\pi} \int_{-\infty}^{\infty} \frac{(\xi - x)[f_{tt}](\xi, t)d\xi}{(\xi - x)^2 + 4h^2} - \frac{1}{\pi} \int_{-\infty}^{\infty} \frac{2h[p_\xi](\xi, t)d\xi}{(\xi - x)^2 + 4h^2}, \tag{28a}$$

$$\langle f_{tt} \rangle(x, t) = -\frac{1}{\pi} \int_{-\infty}^{\infty} \frac{[p_\xi](\xi, t)d\xi}{\xi - x} + \frac{1}{\pi} \int_{-\infty}^{\infty} \frac{(\xi - x)[p_\xi](\xi, t)d\xi}{(\xi - x)^2 + 4h^2} + \frac{1}{\pi} \int_{-\infty}^{\infty} \frac{2h[f_{tt}](\xi, t)d\xi}{(\xi - x)^2 + 4h^2}, \tag{28b}$$

where the square and angled brackets are defined by Eq. (11).

C. The normal stress balance and model simplification

When the above scalings are applied to the normal stress balance on the interface, we recover the linearized, non-dimensional Young-Laplace equation across each interface. This relates the liquid pressures $p^{\pm}$ to the gas pressure P and has the form

$$p^{\pm} - P = \mp \frac{\varepsilon}{We} f_{xx}^{\pm}, \tag{29}$$

where the Weber number $We = \rho_l U_0^2 R/\sigma$ measures the importance of surface tension, and the change in sign on the right-hand side is due to a normal vector pointing out of each liquid phase. Notice, for each x -station the gas pressure close to the droplet free-surface equals the gas pressure close to the layer free-surface as the result of Eq. (15c).

For the experiments of Thoroddsen *et al.*,[1] the Weber number lies between 6 and 360. For ε small, this means surface tension effects are initially small and only really become significant in the final moments before impact when the surface curvature is very large and appears to tend towards a cusp. For the remainder of this paper, we shall

investigate the problem in the absence of surface tension ($\widehat{We} \gg 1$). In this case the simplified normal stress balance across the liquid-gas interface requires $P = p^{\pm}$, where we now take P to be the common pressure in the gas and at the droplet and liquid layer interfaces. With this simplification, the lubrication Equation (20) is unchanged and the integral equation (28b) reduces to

$$\langle f_{tt} \rangle (x,\, t) = \frac{1}{\pi} \int_{-\infty}^{\infty} \frac{2h[f_{tt}](\xi,\, t) d\xi}{(\xi - x)^2 + 4h^2}. \tag{30}$$

Using properties of singular integral equations,[34] Eq. (28a) can be inverted to give

$$[f_{tt}](x,\, t) = -\frac{1}{\pi} \int_{-\infty}^{\infty} \frac{\{2P_{\xi}(\xi,\, t) - I(\xi,\, t)\} d\xi}{\xi - x}, \tag{31a}$$

where

$$I(x,\, t) = \frac{1}{\pi} \int_{-\infty}^{\infty} \frac{(\xi - x)[f_{tt}](\xi,\, t) d\xi}{(\xi - x)^2 + 4h^2}. \tag{31b}$$

In conjunction with the far-field conditions (17), the Eqs. (20) and (31) form a system of two equations relating the pressure P to the difference in height between the two free surfaces $[f]$. Having determined $[f]$, Eq. (30) then allows us to determine the sum of the free-surface heights $\langle f \rangle$ and subsequently find the position of each interface.

D. Compressibility effects in the gas

The lubrication scalings (Eq. (13)), applied to the equation of state (7), imply

$$\rho = \left(1 + \varepsilon^{-1} K P\right)^{1/\gamma}, \quad \text{or} \quad P = \frac{1}{\varepsilon^{-1} K} (\rho^{\gamma} - 1). \tag{32}$$

When substituted into the lubrication Equation (20),

$$12\left(\left(1 + \varepsilon^{-1} K P\right)^{1/\gamma} [f]\right)_t = \left(\left(1 + \varepsilon^{-1} K P\right)^{1/\gamma} [f]^3 P_x\right)_x. \tag{33}$$

For $K \ll \varepsilon$, this gives a simplified lubrication equation

$$12[f_t] = ([f]^3 P_x)_x, \tag{34}$$

which corresponds to an incompressible gas flow and is valid for impact velocities

$$U_0 \ll \frac{p_0^{3/7} \mu_g^{1/7}}{\rho_l^{4/7} R^{1/7}}, \tag{35}$$

above which compressibility effects start to become significant in the gas film. The range of impact velocities for which the air film can be considered incompressible are shown in Figure 3 (and bounded above by the solid line), for $p_0 = 10^5$ Pa. The compressible limit of the problem (assuming the effects of viscous dissipation and thermal diffusion are small) is given by Eq. (33) with $\varepsilon^{-1} K = O(1)$ and is described by Mandre *et al.*[15,32] for droplet impacts with a rigid wall.

If viscous dissipation and thermal diffusion are retained, then the gas density depends upon temperature and the scaled ideal gas law (Eq. (3)) can be written as

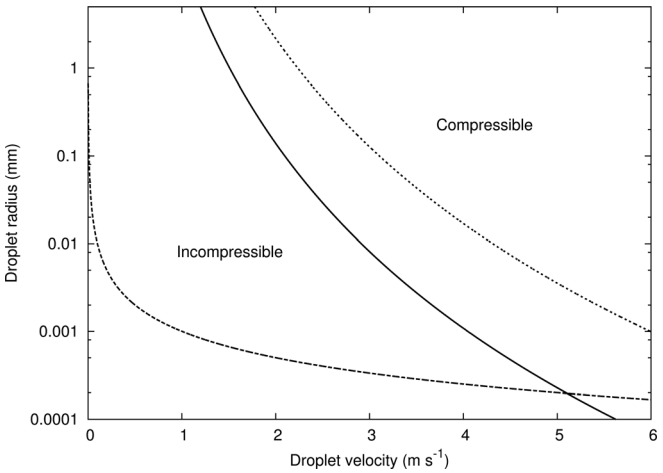

FIG. 3. Regime diagram indicating the different types of compressible behavior for droplet radius and approach speed for an air-water impact at an ambient pressure $p_0 = 10^5$ Pa. The solid curve corresponds to $K = \varepsilon$ and divides the incompressible regime (below the line) from the compressible regime. The dashed line results from the second inequality in Eq. (22), and we must be above this line to have a lubrication equation governing the air flow. The dotted curve corresponds to $\Theta = \varepsilon$, below which the gas density is independent of temperature.

$$\rho = \frac{1 + \varepsilon^{-1} K P}{1 + \varepsilon^{-1} \Theta T}, \tag{36}$$

where the non-dimensional temperature T is related to its dimensional counterpart and a reference temperature T_0 through

$$\bar{T}_g = T_0 + \frac{\rho_l U_0^2}{\varepsilon [\rho_g] c_{v,g}} T. \tag{37}$$

Here the ratio of the temperature increase induced by pressure changes generated by the droplet impact to the ambient temperature,

$$\Theta = \frac{\rho_l U_0^2}{[\rho_g] c_{v,g} T_0}. \tag{38}$$

In this more general case, if $\varepsilon^{-1}\Theta \ll 1$, the gas density is independent of temperature and the mass and momentum conservation equations can be solved independently of the energy conservation equation. Written as a restriction on the approach velocity, this means the incompressible theory holds if

$$U_0 \ll \min\left(\frac{T_0^{3/7} c_{v,g}^{3/7} [\rho_g]^{3/7} \mu_g^{1/7}}{\rho_l^{4/7} R^{1/7}}, \frac{p_0^{3/7} \mu_g^{1/7}}{\rho_l^{4/7} R^{1/7}}\right), \tag{39}$$

when combined with the restriction (Eq. (35)). The additional upper bound to the incompressible regime given by this restriction is shown by the dotted line in Figure 3 for $T_0 = 300$ K. For experiments conducted close to standard atmospheric conditions with common pairs of fluids, it is the former limit arising from considering changes in pressure that provides the most stringent restriction on the applicability of the incompressible theory. The compressible regimes in the small thermal diffusion and dissipation limit and also

in the more general case are discussed briefly in Appendix. However, our focus here is on the lower velocity range where compressibility is negligible. All the results that follow in the main text relate to the incompressible regime.

III. DROPLET IMPACTS WITH LIQUID LAYERS

The evolution of the upper and lower free-surfaces together with the corresponding pressure profiles are shown in Figure 4, for $h=0$, 0.2, 1, 5, and h large. In all cases, the deformation of the two free surfaces act to delay the moment of touchdown beyond $t=0$, the point at which touchdown would occur in the absence of cushioning. This process can be understood by considering the similarities between a lubricating squeeze film and the lubrication behavior given by Eq. (34) or its compressible counterpart. Like a traditional squeeze film, as the droplet approaches the liquid layer, the pressure in the narrowing air gap rises. However, unlike a traditional squeeze film, the droplet and layer interfaces are able to respond in reaction to increased pressures, with the higher pressure in the air gap acting to deflect the free-surfaces, widening the gap between the drop and the layer. Initially the droplet has a single free-surface minimum directly below the center of the droplet. However, as the gap between the droplet and layer narrows, the free-surfaces deform and the fluid in the droplet closest to the gas is decelerated. Mass conservation and the higher speed of the bulk droplet material forces liquid in the droplet out sideways. This material interacts with the pressure profile and leads to the formation of a pair of symmetric minima moving away from this point. Corresponding free-surface maxima exist at the same horizontal position in the layer and the pressure maxima now occur where the separation between free-surfaces is least.

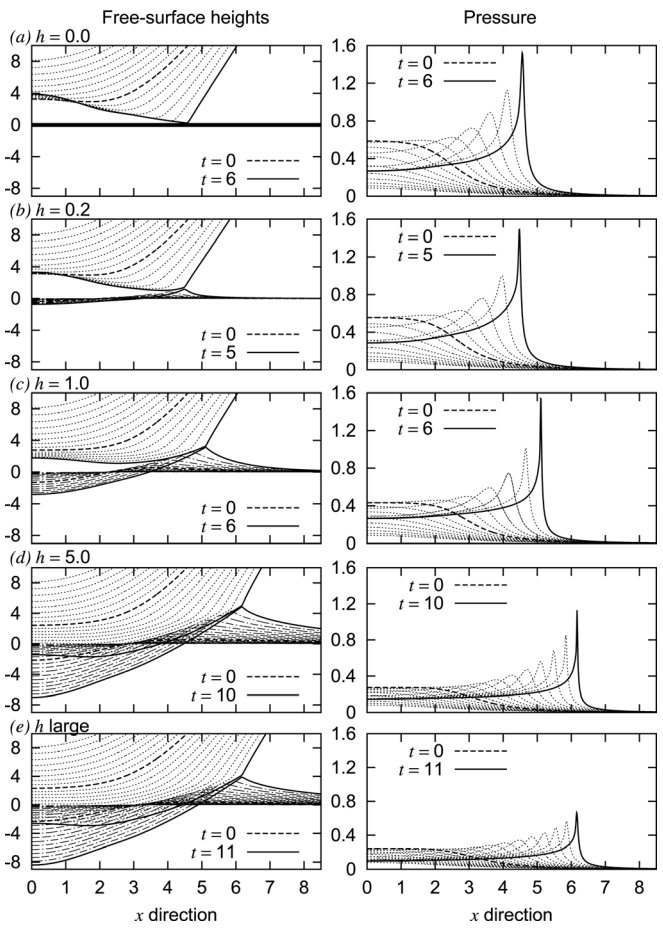

FIG. 4. Air cushioning in two-dimensional droplet impacts with a liquid layer with depth (a) $h=0$, (b) $h=0.2$, (c) $h=1$, (d) $h=5$, and (e) $h\to\infty$.

In Figure 4, the rigid impermeable base of the liquid layer is located at $-h/\varepsilon$ on the vertical axis of the free-surface plots. The degree of deformation occurring in the lower free-surface rises (falls) as the thickness of the layer increases (decreases), and, conversely, the deformation of the upper free-surface decreases (increases). The compliance of the liquid layer decreases with thickness as the presence of the base becomes ever more prominent. This is because liquid in the layer can be more readily displaced by the oncoming droplet when the base is a long way from the free surface. If the layer is shallow, then liquid mass conservation requires that the vertical motion induced in the liquid layer is transferred into horizontal motion, which makes it harder to move the liquid layer out of the path of the droplet and leads to a reduction in the liquid layer free-surface deformation. The initial response of liquid in the layer to an increased gas pressure is to attempt to move vertically way from the high pressure. However, if the liquid layer is shallow, then the rigid base prevents the downward motion of the fluid. This trend is also seen in the pressure profile, where the maximum pressure reduces as h increases. This is because the pressure required to move the layer out of the path of the incoming droplet falls as the space available for the layer to be displaced into rises.

A liquid layer height above the initial undisturbed level corresponds to a transfer of momentum to the liquid layer. Mass conservation indicates the liquid in the layer is moved from below the center of the droplet, sideways, and outwards. This can be seen most readily in a deep liquid layer and may be thought of as the initial stages of the sideways liquid jetting which ultimately leads to splashing. In a shallow liquid layer, the free-surface deformations are larger in the droplet than the liquid layer. However, in conjunction with the reduction in vertical velocity associated with air cushioning, horizontal momentum is also given to the droplet, which again may be a precursor to the splash. If the horizontal momentum gained from air cushioning is ultimately carried into the splashing phase of the impact, then we would expect the ejecta from a droplet impact with a deep liquid layer to initially consist predominantly of layer material as this has the greatest horizontal momentum. Conversely, in a droplet impact with a shallow liquid layer we would expect the splash ejecta to consist primarily of droplet material: the greatest source of horizontal momentum in this case.

To quantify the relationship between the horizontal momentum in the droplet and the layer depth, it is helpful to consider the horizontal component of the liquid acceleration in the droplet, u_t as given by Eq. (21b). By differentiating the scaled droplet mass and momentum equations (21), one can show $u_t(x,y,t)$ and $p_y(x,y,t)$ also satisfy the Cauchy-Riemann equations. Therefore, proceeding as in Sec. II B, a complex function

$$W(x+iy,\,t)=p_y(x,\,y,\,t)+iu_t(x,\,y,\,t), \tag{40}$$

is constructed. If we consider a contour integral around just the droplet free-surface, then the horizontal acceleration in the droplet interior

$$u_t(x, y, t) = -\frac{1}{2\pi}\int_{-\infty}^{\infty} \frac{(\xi - x)p_y^+(\xi, t)d\xi}{(\xi - x)^2 + y^2}, \tag{41}$$

as the horizontal acceleration of the droplet free-surface is zero to leading order. From our results, it is clear that a droplet hitting a dry rigid surface is decelerated more rapidly than a droplet of equivalent size and impact velocity hitting a water layer (see Figure 4, where at $t = 0$ the downward progress of the free-surface of a drop impacting a liquid layer is greater than in the dry case). The vertical deceleration of the droplet is related to the vertical pressure gradient through the momentum equation (21c). Therefore from Eq. (41), the horizontal acceleration and momentum of liquid going into the jet is largest when the deceleration of the droplet occurs most rapidly.

Further insight can be gained by considering the limiting cases of a very deep liquid layer $h \gg 1$ and a very shallow liquid layer $h \ll 1$. These cases are now considered in the next sections.

A. The large h limit

For $h \gg 1$, the depth of the liquid layer is large compared to the horizontal extent of the gas filled gap, so that

$$\varepsilon R \ll H, \tag{42}$$

where H is the dimensional, undisturbed liquid layer depth. In this limit, as $h \to \infty$, the integral $I \to 0$. Therefore,

$$[f_{tt}] = -\frac{2}{\pi}\int_{-\infty}^{\infty} \frac{P_\xi(\xi, t)d\xi}{\xi - x}. \tag{43}$$

In this limit the integral on the right-hand side of Eq. (30) also is negligible, resulting in $\langle f_{tt}\rangle = 0$. This, together with Eq. (43), allows us to explicitly determine the location of each interface.

Equivalently, the same result can be derived by considering each fluid domain separately. In a liquid layer whose depth is much greater than the droplet radius, we can integrate round a semi-circle contour in both the droplet and the liquid layer. As the radius of the semi-circle gets large, the contribution from the arc of the semi-circle is negligible and

$$f_{tt}^{\pm} = \mp\frac{1}{\pi}\int_{-\infty}^{\infty} \frac{P_\xi(\xi, t)d\xi}{\xi - x}. \tag{44}$$

Equation (43) now follows immediately as $[f] = f^+ - f^-$.

The results for a deep liquid layer depth are shown in Figure 4(e). The deep liquid layer depth shows the maximum deflection of the liquid layer free-surface and the least deformation of the droplet free-surface.

B. The small h limit

Less trivial is the small h case, where the depth of the liquid layer is much smaller than the horizontal extent of the gas filled gap. In this limit

$$\varepsilon R \gg H, \tag{45}$$

where H is the dimensional, undisturbed liquid layer depth. Fourier Transforms of the integral equations (30) can be written as

$$2\widehat{P}_x(k, t) = -i\,\mathrm{sgn}(k)\left(1 + e^{-\beta|k|}\right)\widehat{[f_{tt}]}(k, t), \tag{46a}$$

$$\widehat{\langle f_{tt}\rangle}(k, t) = e^{-\beta|k|}\widehat{[f_{tt}]}(k, t), \tag{46b}$$

where $\beta = 2h$ is defined to expedite the analysis.

For $\beta \ll 1$, expansions of the form

$$\widehat{\langle f_{tt}\rangle} = \widehat{\langle f_{tt}\rangle}_0 + \beta\widehat{\langle f_{tt}\rangle}_1 + \beta^2\widehat{\langle f_{tt}\rangle}_2 + \cdots, \tag{47a}$$

$$\widehat{[f_{tt}]} = \widehat{[f_{tt}]}_0 + \beta\widehat{[f_{tt}]}_1 + \beta^2\widehat{[f_{tt}]}_2 + \cdots, \tag{47b}$$

$$\widehat{P}_x = \widehat{P}_{x0} + \beta\widehat{P}_{x1} + \beta^2\widehat{P}_{x2} + \cdots, \tag{47c}$$

are substituted into the Fourier transformed integral equations (46). Equating the terms of the resulting expansion at leading order implies,

$$2\widehat{P}_{x0} = -2i\,\mathrm{sgn}(k)\widehat{[f_{tt}]}_0, \tag{48a}$$

$$\widehat{\langle f_{tt}\rangle}_0 = \widehat{[f_{tt}]}_0. \tag{48b}$$

The application of an inverse Fourier transform to Eq. (48b) gives $f_{tt0}^- = 0$. Together with the far-field condition $f^- \to 0$, as $|x| \to \infty$, this implies $f_0^- = 0$. Subsequently, an inverse Fourier transform, applied to Eq. (48a), implies

$$f_{tt0}^+ = -\frac{1}{\pi}\int_{-\infty}^{\infty} \frac{P_{\xi 0}d\xi}{\xi - x}, \tag{49}$$

indicating the leading order behavior for small β is the same as droplet impact with a solid wall.

After some simplification, the next order correction (given by equating terms at order β) implies

$$2\widehat{P}_{x1} = -2i\,\mathrm{sgn}(k)\widehat{[f_{tt}]}_1 + ik\widehat{f_{tt}^+}_0, \tag{50a}$$

$$2\widehat{f_{tt}^-}_1 = -|k|\widehat{f_{tt}^+}_0. \tag{50b}$$

If we take an inverse Fourier transform of Eq. (50b), then we find

$$f_{tt}^-{}_1 = \frac{1}{\pi}\frac{\partial}{\partial x}\int_{-\infty}^{\infty} \frac{f_{tt}^+{}_0 d\xi}{\xi - x}. \tag{51}$$

From Eq. (49) and properties of singular integral equations,[34] it follows immediately that

$$f_{tt}^-{}_1 = P_{xx0}, \tag{52}$$

which gives the first correction to the lower free-surface in this case. A similar relationship between the free-surface height and the pressure holds for the air cushioning of solid bodies coated by shallow liquid layers.[35]

The leading order behavior for small h is shown in Figure 5(a) and is identical to the case of droplet impact with a solid wall. This figure shows the maximum deformation of

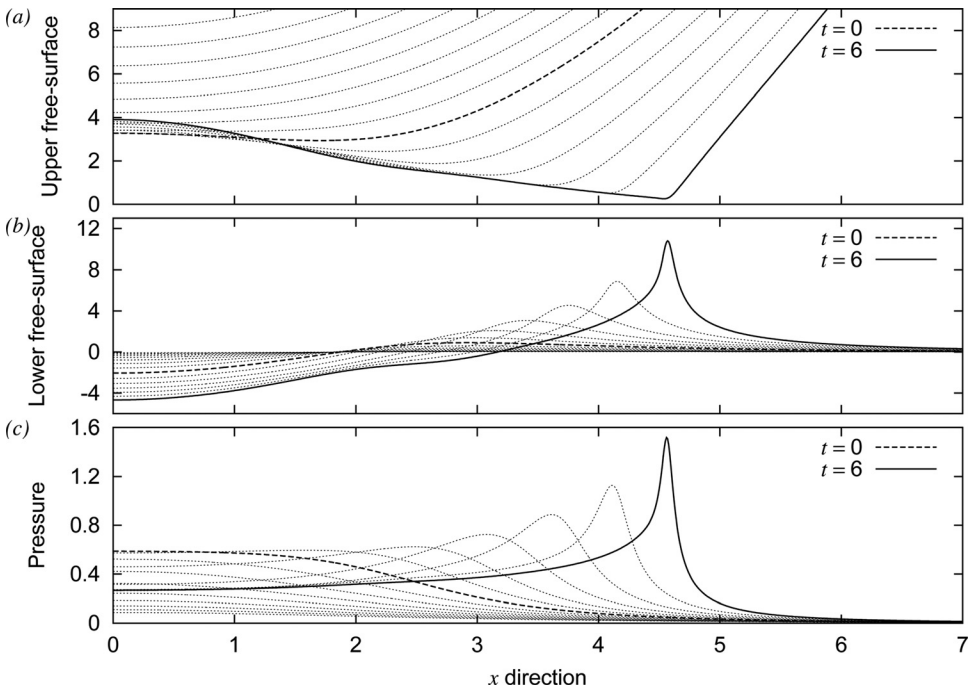

FIG. 5. Air cushioning in two-dimensional droplet impacts with a shallow liquid layer. (a) shows the upper free-surface, (b) the lower free-surface, and (c) the pressure. The upper free-surface and the pressure evolution are the same as those shown in Figure 4(a) for droplet impact with a solid wall.

the droplet free-surface and the largest pressures at each integer time-step of the five layer depths considered. The correction to the lower free-surface at next order is shown in Figure 5(b), alongside the droplet free-surface and the air layer pressure. The deformation of the liquid layer free-surface is $O(\varepsilon)$ times smaller than the deformations experienced by the droplet free-surface. However, like the droplet free-surface, the liquid layer free-surface initially deflects away from the incoming droplet, before forming a pair of peaks some horizontal distance away from the point below the center of the droplet. The position of these peaks matches the minima belonging to the droplet free-surface, and it is at these points (where the pressure is greatest) that initial touchdown will most likely occur, again leading to the trapping of a gas bubble.

IV. TRAPPED BUBBLE SIZE

The amount of gas trapped between the droplet and layer as impact occurs depend upon the approach speed U_0, the droplet radius R, and the depth of the liquid layer H. In a model using two spatial dimensions quantitative comparisons cannot be made with droplet impacts, which are inherently three-dimensional. However, we can determine a qualitative relationship between the layer depth and the amount of trapped gas. In their investigation of three-dimensional droplet impacts with a solid wall using a similar scaling regime as employed here and again assuming the gas to be incompressible, Hicks and Purvis[18] find that the three-dimensional bubble volume V depends on the droplet radius and approach speed through

$$V = \frac{\mu_g^{4/3} R^{5/3}}{\rho_l^{4/3} U_0^{4/3}} \tilde{V}, \tag{53}$$

where the numerically computed prefactor, $\tilde{V} = 94.48$. The layer depth H is absent in this scaling as only droplet impacts with solid surfaces were considered.

Gas flow in the lubrication layer is driven by the pressure gradient with the result that the gas trapped between the pressure peaks is restricted from escaping. Therefore, we can estimate the two-dimensional bubble area by integrating the amount of gas trapped between the upper and lower free-surfaces and the horizontal location of the maxima of the pressure field. Symmetry in the profiles about $x = 0$ implies the area of the two-dimensional bubble trapped is

$$\tilde{V}(t) = 2 \int_0^{x_p} [f](\xi, t) d\xi, \tag{54}$$

where x_p is the horizontal station corresponding to the maximum pressure. Clearly, as the free-surface evolves over time the value of $\tilde{V}(t)$ changes, starting from zero early in the droplet approach when only one pressure maximum exists and approaching a maximum as the distance between the two free-surfaces tend to zero. During the numerical solution of the model equations touchdown is never reached, but we approximate this by evaluating Eq. (54) when the separation $[f] = 0.185$. The free-surface position becomes more computationally expensive to calculate for h small, and this value of the separation is the smallest achievable across the range of values of h shown in Figure 6.

Figure 4 shows the profiles of the upper and lower free-surfaces for a range of values of layer depth h. This shows that the free surface profiles have a clear dependence upon h; therefore with a liquid layer present different values of h would generate different values of the prefactor $\tilde{V}$. The dependence of $\tilde{V}$ on h is shown in Figure 6, and we see an increase in the layer depth h corresponds monotonically to an increase in bubble volume. This is because the liquid layer free-surface is most compliant and able to deform when interactions between it and the rigid base of the liquid layer are least. This occurs when the base of the liquid layer is a long way from the liquid layer free-surface as a result of the mechanism described in Sec. III.

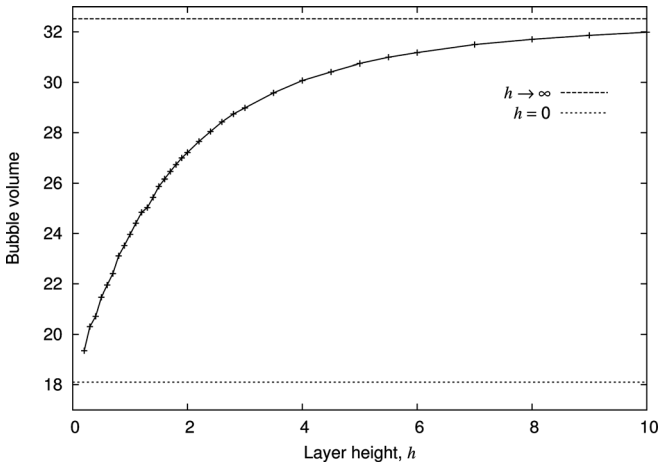

FIG. 6. Bubble volume as a function of layer depth h, when $[f] = 0.185$. The horizontal lines indicate the bubble volume at the same point for impact with a solid and impact with deep liquid.

Equation (53) shows good agreement with the trends shown and the limited measured bubble volumes in the experiments for droplet impact with a solid,[3,4] with the volume of the gas bubble trapped increasing with bubble radius and decreasing with impact speed.[18] Very limited experimental results exist which allow comparison of the bubble volume with the liquid layer depth. A comparison of droplet impact experiments into deep water and a solid surface[3] indicates that the average thickness of the gas film of 1–2.5 μm in impacts with a liquid, compared to 2–5 μm for impact with a solid. For this comparison the average gas film thickness was found by dividing the final bubble volume by the area of the trapped gas film. Thoroddsen *et al.*[3] suggest the reason for the difference in average gas film heights is due to the increased compliance of the liquid layer free-surface (compared to a rigid body), which allows more time for gas to drain from the film. In contrast, in our two-dimensional numerical study, the bubble volume divided by the air film radius gives an average non-dimensional film thickness of 5.37 in impacts with a deep liquid-layer and 3.81 in impacts with a solid surface. Therefore, we find that the increased compliance of both the droplet and layer free-surfaces allows a larger bubble to be trapped. Several factors may contribute to this difference in behavior; the numerical results presented are for an idealized two-dimensional impact problem. Additionally, in the experiments with greatest droplet approach speeds, $K/\varepsilon = O(1)$, indicating compressibility effects may be significant in the gas film. These compressibility effects are not included in the comparison for simplicity and may account for part of the discrepancy. However, if compressible effects are included, then the scaling of the bubble volume (Eq. (53)) is unchanged, although the calculated value of $\tilde{V}$ may change significantly. Other factors such as surface tension may affect the bubble volume, and further experimental results for a range of layer depths would be useful to enable better comparison between theory and experiments.

V. DROPLET-DROPLET IMPACTS

The model of Sec. III A, in which the liquid layer is very deep, can easily be generalized to consider the problem of air cushioning in impacts between two droplets. In a frame of reference in which an upper droplet of radius R and velocity U_0 approaches a second, lower stationary droplet of radius R', the evolution of the two free-surfaces is governed by Eq. (44), coupled to the lubrication Equation (34). Here gas compressibility effects are again assumed to be negligible.

A. Head on collisions

If the moving droplet is traveling along the line joining the centers of mass of the two droplets, then a head on collision will result. In this case the far-field conditions are given by

$$f^+ \sim \frac{x^2}{2} - t, \quad f^- \sim -\frac{x^2}{2\alpha^2}, \quad \text{and} \quad P \to 0, \ \text{as} \ |x| \to \infty, \tag{55}$$

with initial conditions given by equality at some large negative t. Here the constant $\alpha = R'/R$. Results are shown in Figure 7 for the cases in which the stationary droplet is four times the size, twice the size, and the same size as the moving droplet, corresponding to $\alpha = 4$, 2 and 1, respectively. The behavior associated with a large moving droplet impacting with a stationary small droplet can be seen by changing the frame of reference to one in which the small droplet appears stationary.

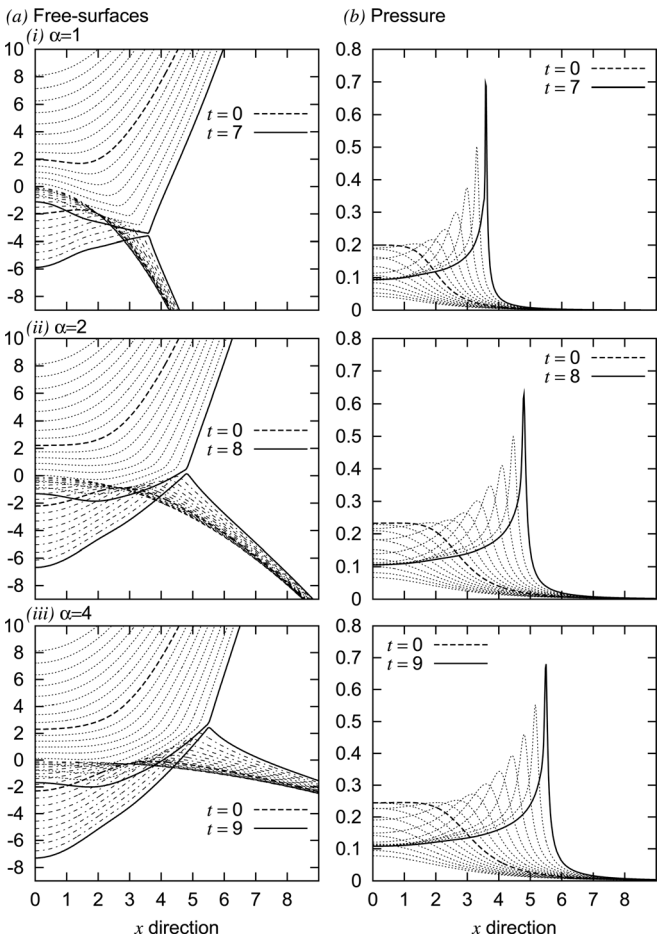

FIG. 7. Air cushioning in two-dimensional droplet-droplet impacts. (a) shows the free-surface profiles and (b) the pressure, for (i) $\alpha = 1$ (the same sized droplets), (ii) $\alpha = 2$, and (iii) $\alpha = 4$.

The resulting free-surface and pressure profiles have many features in common with droplet impacts with liquid layers (see Sec. III) and solids.[14] Again we see the highest initial pressures at the point where the separation between the two droplets is least. The build up of pressure acts to decelerate the moving droplet and deflect the free surfaces of both droplets away from impact. As the liquid in the droplet closest to the point of impact is decelerated the remaining fluid in the droplet is forced out sideways to preserve mass conservation and again this leads to new free-surface minima some distance away from the common axis. These new locations with smallest separation again correspond to maxima in the pressure profiles. Through this mechanism, air-cushioning acts to delay the instant of initial impact.

The free-surface profiles generated are also strongly reminiscent of those generated in the slower speed droplet coalescence problem with viscous film drainage.[28,29] In this problem the viscous fluid in the gap separating the two droplets must be drained prior to touchdown. Surface tension effects are more prominent at lower speeds due to smaller corresponding Weber number. However, the description of the mechanism governing the evolution of the droplet free-surfaces is largely the same, with the proviso that viscous effects dominate in the droplet bulk at lower speeds.

In the air cushioning context the free-surface profiles again strongly suggest gas bubble entrapment during impact. To our knowledge, gas bubbles have not been observed experimentally in violent droplet collisions. However, given the necessary difficulties with high-speed photography and the motion of a pair of droplets, such experiments would be dramatically more difficult to accomplish than either droplet impact with a solid or a stationary liquid layer.

Figure 7 shows droplet collisions for two equal droplets and for collisions in which $\alpha = 2$ and 4. These show that as one of the droplets is increased in size, both the time to initial touchdown and the size of the gas bubble trapped are increased. This is because the lower curvature of the free surface of the larger droplet is more compliant to the increases in pressure and is therefore able to deform faster and further, mimicking the behavior seen in droplet impacts with layers of increasing depth.

B. Glancing collisions

In many cases, rather than a head on collision between two droplets, the droplets will be involved in a glancing impact. In this case, we shall restrict our attention to collisions between droplets that initially have the same radius R. However, the model can be generalized as in the previous section to describe glancing impacts between different sized droplets.

For clarity we adopt a frame of reference in which the droplets would impact at $x = y = t = 0$ if they did not deform and in which both droplets move towards impact with a non-dimensional speed of one half. We consider a horizontal droplet separation between the centers of the two droplets given by d. In this case the far-field conditions are given by

$$f^+ \sim \frac{x}{2}\left(x + \frac{d}{2}\right) - \frac{t}{2}, \quad f^- \sim -\frac{x}{2}\left(x - \frac{d}{2}\right) + \frac{t}{2},$$
$$\text{and} \quad P \to 0, \quad \text{as} \quad |x| \to \infty. \tag{56}$$

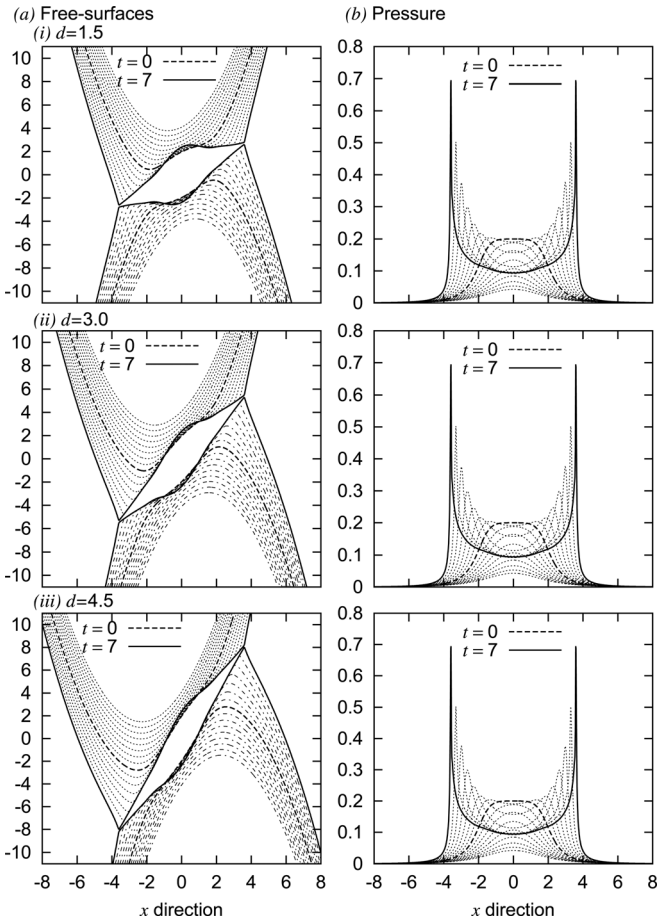

FIG. 8. Air cushioning in two-dimensional droplet-droplet impacts. (a) shows the free-surface profiles and (b) the pressure, for a horizontal offset (i) $d = 1.5$, (ii) $d = 3.0$, and (iii) $d = 4.5$.

For large negative times we assume the droplets are undeformed with $P = 0$ for all x.

Figure 8 shows the free-surface and pressure evolution for the cases (i) $d = 1.5$, (ii) $d = 3.0$, and (iii) $d = 4.5$. Even with glancing impacts we still predict a gas bubble will be trapped as impact is approached, although we must note that the model used to calculate these impacts describe a region $O(\varepsilon)$ away from head-on collisions between droplets. Therefore, other behavior may be possible for larger horizontal separations. However, for these small horizontal offsets we note that the pressure profiles are remarkable similar in all cases. This can be explained by the fact that in the far-field, the gap width $[f]$ is independent of d. Therefore, as the lubrication equation is written in terms of $[f]$ rather than each explicit free-surface position, we should expect the same pressure profile at each integer time-step. The corresponding bubble volume is also the same size in all cases, with the skewed gas pocket becoming longer and narrower as d increases.

VI. CONCLUSIONS

A model has been developed to describe the air cushioning of liquid droplets during an impact with a finite depth liquid layer. Central to this model is the coupling of a relationship governing the free-surface evolution of an

inviscid droplet to a thin film lubrication model of the gas. The contour integration described, while previously used in the study of ground effects[33,36] and post impact droplet free-surface evolution in the absence of air,[22] has now been coupled to an interactive description of the air, allowing gas pressure induced free-surface deformation and air cushioning. The behavior of the gas film is governed by a canonical squeeze film problem, albeit one in which the free surfaces of the gas film are able to deform when the pressure in the film increases.

For a droplet with dimensional radius R, the horizontal interaction distance between the droplet and the gas film is of size εR, where ε is defined by Eq. (14). This length scale is used to identify a key parameter in the modeling, $h = H/\varepsilon R$, which is the ratio of the liquid layer depth to the horizontal interaction distance. For $h \ll 1$, the liquid layer is shallow and ultimately the droplet free-surface and pressure profiles tend towards those seen in droplet impacts with solid surfaces. In this limit the liquid layer is flat to leading order. However, the first order correction is calculated and this allows higher-order deformations of the liquid layer free-surface. For $h \gg 1$, the liquid layer is deep and the free-surface and pressure profiles tend towards those found in an infinite liquid layer. The free-surface deformations are largest in the droplet in the former case and are largest in the liquid layer in the latter. This is because the presence of the rigid impermeable base below the liquid layer restricts the ability of the liquid layer to be pushed out of the path of the droplet. In impacts with a shallow liquid layer the majority of the horizontal momentum given to the liquid occurs in the droplet, while, conversely, in impacts with a deep water layer the majority of the horizontal momentum arises in the liquid layer. If this horizontal momentum is carried through into the liquid jetting and splashing phases of the impact, then this suggests the ejecta initially comes primarily from the droplet in an impact with shallow water and from the liquid layer in an impact with deep water.

It is interesting to compare these predictions to the splash jet composition which results from existing theories of droplet impact, available when air effects are neglected. Asymptotic theories of droplet impact predict that the contributions to the splash jet from the layer and the droplet are equal due to symmetry for non-dimensional times $t \ll (H/R)^{2/3}$ after impact,[23] with the jet exactly dividing the gap between droplet and layer due to symmetry. In this regime the small droplet penetration depth means the effect of the bottom of the liquid layer is not felt. When air cushioning is neglected, the liquid layer is at rest and the droplet has uniform velocity until impact. Impact then occurs at a single point directly below the center of the droplet. With air cushioning included, horizontal momentum is imparted to both the layer and the droplet prior to touchdown. It is reasonable to expect that the fluid with the greater initial horizontal momentum upon impact will provide a greater proportion of the jet material as it is able to initially carry more material into the jet. Therefore with air effects included, we would expect a greater proportion of the initial splash jet to come from the layer as the layer depth increases. In a droplet impact with a rigid solid, clearly all the material in the splash jet must come from the droplet as there is no liquid layer. In this case, the asymptotic theory for small times after impact produces a mixed-boundary value problem, which predicts that the jet runs along the solid surface,[19,20] as seen in experiments conducted at low ambient gas pressures.[37] At higher ambient gas pressures, the subsequent interactions with air then causes the liquid jet to detach from the solid surface and lift up into the air, ultimately leading to the formation the characteristic splash corona.

Also of interest are recent experiments of droplet impacts with a spinning disk.[38,39] For a range of horizontal substrate translation speeds, the liquid jet moving in the direction of the disk spreads along the surface, while in the opposite direction the liquid jet lifts off the disk to form a partial splash corona. However, the small-time asymptotic solution of the corresponding mixed-boundary value problem for oblique impacts again predicts liquid jets running along the solid surface in all directions.[40] The subsequent post-impact lift off of the liquid jet moving in the opposite direction to the substrate is seemingly due to interactions between the liquid jet and the viscous boundary layer in the gas induced by the substrate motion. The higher relative velocity resulting from the liquid jet moving against the viscous gas boundary layer produces a higher local pressure forcing the jet upwards to create the splash. Conversely, where the liquid jet and the viscous gas boundary layer are moving in parallel, there is a much lower relative velocity and resultant pressure, which allows the jet to spread over the surface. This is consistent with the splashing (spreading) behaviour seen in normal droplet impacts at high (low) pressure.[37]

Open questions remain regarding key features of air cushioning in droplet impact. It is still unclear whether touchdown occurs in finite time within the current modeling regime. We have found no numerical evidence of touchdown here, in common with studies of droplet impacts with a rigid body in both the incompressible[14] and compressible[15] regimes. For impact with a dry wall, models in the compressible regime predict that the droplet spreads on an air cushion,[15] while in the incompressible regime there is a local similarity solution to the model equations found by assuming touchdown occurs. However, it is unclear if this similarity solution is ever obtained in calculations. Most likely, additional physics is required to allow the model to reach touchdown in both cases. Recent studies[32] have shown some of that terms neglected in the horizontal momentum equation (15b), can also become significant just prior to impact when the gas film thickness is less than 100 nm. Additionally, in this regime, intermolecular forces, heat transfer, capillary waves, or interfacial instabilities may generate other secondary phenomena such as Mesler entrainment,[5,6] which are not explained by the existing theory. It is expected that including these additional physical effects will improve comparison with experiments[1,3] and may in addition provide new insight into the actual initial touchdown and coalescence phase of the impact. Further work is also required to assess the stability of the free surfaces as impact is approached, particularly when the surface curvature becomes very large. For higher momentum droplet and other liquid impacts in which the

Reynolds number is greater than $O(10^7)$, gas compressibility has not previously been incorporated into the inviscid gas film which results in that case. Incorporating this effect will further understanding in a range of physical problems: not just only very high momentum droplet impacts, but also ship slamming and wave impacts.

ACKNOWLEDGMENTS

The authors are very grateful for the support of the EPSRC (EP/E027814/1) and the Nuffield foundation (NAL/32574).

APPENDIX: COMPRESSIBLE GAS FILM REGIMES

With compressibility effects retained and the effects of thermal diffusion and dissipation in Eq. (4) neglected, the behavior of the gas film is governed by Eq. (33). Depending on the size of $K = \rho_l U_0^2/p_0$, there are three cases to consider. These correspond to $K \ll \varepsilon$ (the incompressible problem discussed in the main text), as well as $\varepsilon^{-1}K = O(1)$, and $\varepsilon \ll K$. For ε defined by Eq. (14), Figure 3 shows the regime diagram covering the different types of compressible gas film for a droplet impact in air of ambient pressure $p_0 = 10^5$ Pa. The solid curve shown corresponds to $K = \varepsilon$ and indicates the division between the different regimes. Also shown by the dashed line in Figure 3 is the condition given by the right-hand inequality of Eq. (22). Above this line, viscous terms in the droplet are not present to leading order. The corresponding condition given by the left-hand inequality results in a condition on the droplet momentum at velocities greater than those shown in Figure 3. Therefore, the viscous gas and inviscid droplet regime is the leading order balance for the early stages of droplet impacts with parameters in the range covered by Figure 3 that lie above the dashed line.

If the approach speed U_0 and ambient pressure p_0 are such that $\bar{K} = \varepsilon^{-1}K = O(1)$, then the lubrication Equation (33) simplifies to

$$12\left((1+\bar{K}P)^{1/\gamma}[f]\right)_t = \left((1+\bar{K}P)^{1/\gamma}[f]^3 P_x\right)_x. \tag{A1}$$

The air-cushioning behavior in this moderately compressible regime is then governed by this compressible lubrication equation in conjunction with the droplet and layer free-surface equations (31) and far-field conditions (16). If the droplet approaches impact with the layer with a higher approach speed and the ambient pressure is such that $\varepsilon \ll K$, then (to leading order) the equation of state (32) can be used to eliminate the pressure gradient in (33) to leave

$$(\rho[f])_t = 0. \tag{A2}$$

Again this equation can be solved in conjunction with the free-surface Equation (31) and far-field conditions (16) to give the air-cushioning behavior in this case. Results in both regimes of compressible air-cushioned droplet impacts with a rigid solid have been presented,[15,32] with both cases predicting that a trapped gas bubble is formed.

If the thermal diffusion and viscous dissipation terms are retained in the energy conservation Equation (4), then after scaling

$$\frac{1}{\gamma-1}\left(\frac{\partial P}{\partial t}+U\frac{\partial P}{\partial x}\right)-\frac{\gamma}{\gamma-1}\frac{\varepsilon K^{-1}+P}{\rho}\left(\frac{\partial \rho}{\partial t}+U\frac{\partial \rho}{\partial x}+V\frac{\partial \rho}{\partial y}\right) = \frac{1}{Pe}\frac{\partial^2 T}{\partial y^2}+\left(\frac{\partial U}{\partial y}\right)^2. \tag{A3}$$

Here Eq. (37) has been used to rescale the temperature, while the reduced Péclet number is defined to be

$$Pe = \frac{\varepsilon^2[\rho_g]c_{v,g}U_0 R}{k_g}. \tag{A4}$$

The terms in the scaled energy equation (A3) are presented in the same order as the terms of its dimensional counterpart Eq. (4), and, consequently, we see immediately that the final term (the leading order contribution from the dissipation term) is of the same size as the terms on the left-hand side and should not be neglected. However, if the conditions $\varepsilon^{-1}K \ll 1$ and $\varepsilon^{-1}\Theta \ll 1$ are met, then the solution of the energy conservation equation uncouples from the lubrication problem, which can be solved independently for the incompressible case.

[1]S. T. Thoroddsen, T. G. Etoh, and K. Takehara, "Air entrapment under an impacting drop," J. Fluid Mech. **478**, 125 (2003).
[2]D. K. Woolf, I. S. Leifer, P. D. Nightingale, T. S. Rhee, P. Bowyer, G. Caulliez, G. de Leeuw, S. E. Larsen, M. Liddicoat, J. Baker, and M. O. Andreae, "Modelling of bubble-mediated gas transfer: Fundamental principles and a laboratory test," J. Mar. Syst. **66**, 71 (2007).
[3]S. T. Thoroddsen, T. G. Etoh, K. Takehara, N. Ootsuka, and Y. Hatsuki, "The air bubble entrapped under a drop impacting on a solid surface," J. Fluid Mech. **545**, 203 (2005).
[4]D. B. van Dam and C. Le Clerc, "Experimental study of the impact of an ink-jet printed droplet on a solid substrate," Phys. Fluids **16**, 3403 (2004).
[5]L. Esmailizadeh and R. Mesler, "Bubble entrainment with drops," J. Colloid Interface Sci. **110**, 561 (1986).
[6]J. Herman and R. Mesler, "Bubble entrainment from bursting bubbles," J. Colloid Interface Sci. **117**, 565 (1987).
[7]H. N. Oğuz and A. Prosperetti, "Bubble entrainment by the impact of drops on liquid surfaces," J. Fluid Mech. **219**, 143 (1990).
[8]J. H. G. Verhagen, "The impact of a flat plate on a water surface," J. Ship Res. **11**, 211 (1967).
[9]S. K. Wilson, "A mathematical model for the initial stages of fluid impact in the presence of a cushioning fluid layer," J. Eng. Math. **25**, 265 (1991).
[10]J. M. Oliver, "Water entry and related problems," Ph.D. thesis (University of Oxford, Oxford, 2002).
[11]R. Purvis and F. T. Smith, "Air-water interactions near droplet impact," Eur. J. Appl. Math. **15**, 853 (2004a).
[12]J.-M. Vanden-Broeck and F. T. Smith, "Surface tension effects on interaction between two fluids near a wall," Q. J. Mech. Appl. Math. **61**, 117 (2008).
[13]J.-M. Vanden-Broeck and F. T. Smith, "Supercritical two-fluid interactions with surface tension and gravity," Mathematika **56**, 93 (2010).
[14]F. T. Smith, L. Li, and G. X. Wu, "Air cushioning with a lubrication/inviscid balance," J. Fluid Mech. **482**, 291 (2003).
[15]S. Mandre, M. Mani, and M. P. Brenner, "Precursors to splashing of liquid droplets on a solid surface," Phys. Rev. Lett. **102**, 134502 (2009).
[16]F. T. Smith and R. Purvis, "Air effects on large droplet impact," AIAA Paper 2005-5184, 2005.
[17]F. T. Smith, N. C. Ovenden, and R. Purvis, "Industrial and biomedical applications," in *Proceedings of IUTAM Symposium on One Hundred Years of Boundary Layer Research, Göttingen, Germany*, edited by G. E. A. Meier, K. R. Sreenivasan, and H.-J. Heinemann (Springer, Berlin, 2006), p. 291.
[18]P. D. Hicks and R. Purvis, "Air cushioning and bubble entrapment in three-dimensional droplet impacts," J. Fluid Mech. **649**, 135 (2010).
[19]S. D. Howison, J. R. Ockendon, and S. K. Wilson, "Incompressible water-entry problems at small deadrise angles," J. Fluid Mech. **222**, 215 (1991).
[20]J. M. Oliver, "Second-order Wagner theory for two-dimensional water-entry problems at small deadrise angles," J. Fluid Mech. **572**, 59 (2007).

[21]A. A. Korobkin, "Shallow water impact problems," J. Eng. Math. **35**, 233 (1999).
[22]R. Purvis and F. T. Smith, "Droplet impact on water layers: Post-impact analysis and computations," Philos. Trans. R. Soc. Lond. A **363**, 1209 (2005).
[23]S. D. Howison, J. R. Ockendon, J. M. Oliver, R. Purvis, and F. T. Smith, "Droplet impact on a thin fluid layer," J. Fluid Mech. **542**, 1 (2005).
[24]C. Pozrikidis, "The deformation of a liquid drop moving normal to a plane wall," J. Fluid Mech. **215**, 331 (1990).
[25]K. L. Pan and C. K. Law, "Dynamics of droplet-film collision," J. Fluid Mech. **587**, 1 (2007).
[26]S. Protière, A. Boudaoud, and Y. Couder, "Particle-wave association on a fluid interface," J. Fluid Mech. **554**, 85 (2006).
[27]J. Eggers, J. R. Lister, and H. A. Stone, "Coalescence of liquid drops," J. Fluid Mech. **401**, 293 (1999).
[28]P. J. A. Janssen, P. D. Anderson, G. W. M. Peters, and H. E. H. Meijer, "Axisymmetric boundary integral simulations of film drainage between two viscous drops," J. Fluid Mech. **567**, 65 (2006).
[29]S. Kaur and L. G. Leal, "Three-dimensional stability of a thin film between two approaching drops," Phys. Fluids **21**, 072101 (2009).
[30]K. Stewartson, *The Theory of Laminar Boundary Layers in Compressible Fluids* (Oxford Clarendon Press, Oxford, 1964).
[31]P. Howell, "Fluid-mechanical modelling of the scroll compressor," *Mathematical Modeling: Case Studies from Industry* (Cambridge University Press, Cambridge, 2001), Chap. I.
[32]M. Mani, S. Mandre, and M. P. Brenner, "Events before droplet splashing on a solid surface," J. Fluid Mech. **647**, 163 (2010).
[33]R. Purvis and F. T. Smith, "Planar flow past two or more blades in ground effect," Q. J. Mech. Appl. Math. **57**, 137 (2004b).
[34]N. I. Muskhelishvili, *Singular Integral Equations: Boundary Problems of Function Theory and their Application to Mathematical Physics*, 2nd ed. (Dover, Mineola, New York, 2008).
[35]A. A. Korobkin, A. S. Ellis, and F. T. Smith, "Trapping of air in impact between a body and shallow water," J. Fluid Mech. **611**, 365 (2008).
[36]M. A. Jones, "Mechanisms in 'wing-in-ground' effect aerodynamics," Ph.D. thesis (University College London, London, 2000).
[37]L. Xu, W. W. Zhang, and S. R. Nagel, "Drop splashing on a dry smooth surface," Phys. Rev. Lett. **94**, 184505 (2005).
[38]L. Courbin, J. C. Bird, and H. A. Stone, "Splash and anti-splash: Observation and design," Chaos **16**, 041102 (2006).
[39]J. C. Bird, S. S. H. Tsai, and H. A. Stone, "Inclined to splash: Triggering and inhibiting a splash with tangential velocity," New J. Phys. **11**, 063017 (2009).
[40]S. D. Howison, J. R. Ockendon, and J. M. Oliver, "Oblique slamming, planing and skimming," J. Eng. Math. **48**, 321 (2004).